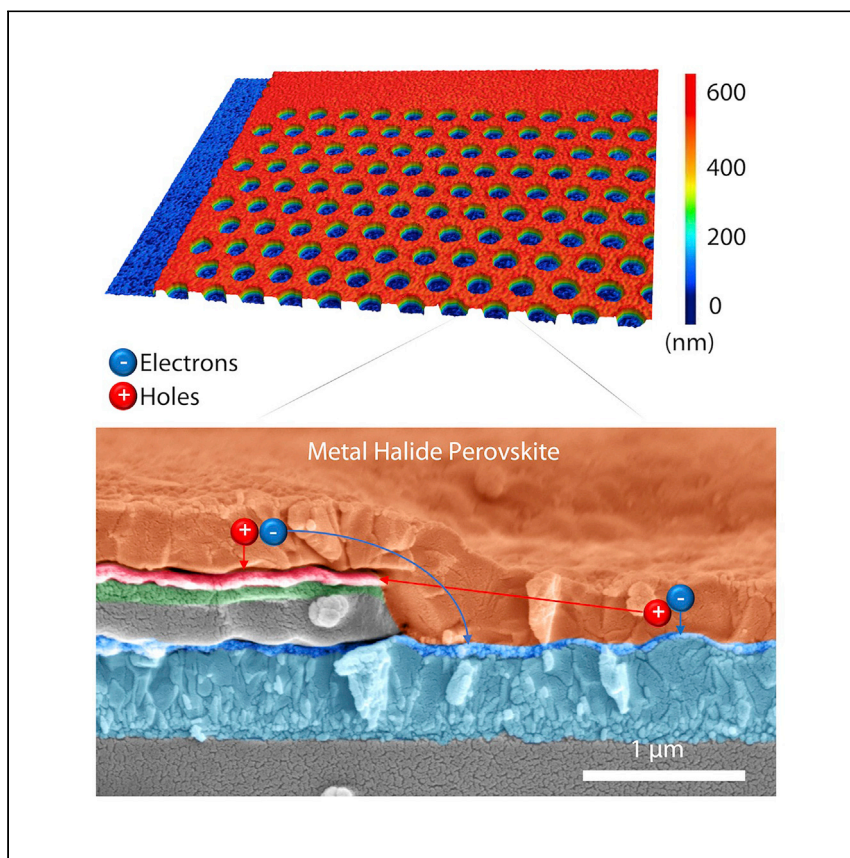


**Article**

# Complementary interface formation toward high-efficiency all-back-contact perovskite solar cells



Perovskite solar cells could revolutionize photovoltaic technology, but peak efficiency is limited in conventional planar architectures and stability remains challenging. Prince et al. highlight the importance of complementary interface formation in all-back-contact electrodes to help enable a new class of highly efficient and stable perovskite solar cell architectures.

Kevin J. Prince, Marco Nardone,  
Sean P. Dunfield, ..., Joseph J.  
Berry, Colin A. Wolden, Lance  
M. Wheeler

[lance.wheeler@nrel.gov](mailto:lance.wheeler@nrel.gov)

## HIGHLIGHTS

Complementary interface formation is critical for all-back-contact electrodes

UV-ozone increased the work function of  $\text{NiO}_x$  and removed residual carbon on  $\text{TiO}_2$

Annealing after UV-ozone reduced hydroxide or defect species in  $\text{NiO}_x$

2D models highlight dependence of carrier collection on interface defect density

Prince et al., Cell Reports Physical Science 2,  
100363  
March 24, 2021  
<https://doi.org/10.1016/j.xcrp.2021.100363>



Article

# Complementary interface formation toward high-efficiency all-back-contact perovskite solar cells

Kevin J. Prince,<sup>1,2</sup> Marco Nardone,<sup>3</sup> Sean P. Dunfield,<sup>1,4</sup> Glenn Teeter,<sup>1</sup> Mirzo Mirzokarimov,<sup>1</sup> Emily L. Warren,<sup>1</sup> David T. Moore,<sup>1</sup> Joseph J. Berry,<sup>1</sup> Colin A. Wolden,<sup>1,2</sup> and Lance M. Wheeler<sup>1,5,\*</sup>

## SUMMARY

All-back-contact (ABC) architectures for perovskite photovoltaics represent untapped potential for higher efficiency and enhanced durability compared to conventional planar architectures. Interface engineering can be more complex in ABC designs, because both the electron and hole transport layers (ETLs/HTLs) are simultaneously exposed during processing. Herein, we fabricate ABC perovskite solar cells with a non-stabilized current-voltage scan power conversion efficiency >10% by developing complementary interface processing. UV-ozone exposure followed by annealing increases the work function and reduces the defect density of the NiO<sub>x</sub> HTL and removed contamination from the TiO<sub>2</sub> ETL, which increases voltage and current collection. We measure the chemical composition of each transport layer interface using photoelectron spectroscopy and then use the resulting trends to inform a two-dimensional drift-diffusion model. The model suggests that further reduction of charged interface defect density, increase in the hole selective contact work function, and passivation of the front surface will enable >20% of ABC devices.

## INTRODUCTION

Metal halide perovskites have established themselves as a transformative material for semiconductor applications due to their unique combination of desirable properties, including strong absorption coefficient,<sup>1–3</sup> low nonradiative recombination rates,<sup>4</sup> long carrier diffusion lengths,<sup>5–7</sup> photon recycling,<sup>8</sup> and low-cost solution processability.<sup>9</sup> These properties position perovskites to revolutionize numerous optoelectronic technologies,<sup>10–13</sup> including widespread photovoltaic (PV) adoption that spans building integrated-PV<sup>14,15</sup> to utility-scale solar cell deployment. Perovskite solar cells (PSCs) have rapidly reached a solar-to-electric power conversion efficiency (PCE) of >25% based on planar architectures.<sup>16</sup> Progress on efficiency and stability for planar architectures has hinged on precise control of interface properties.<sup>17,18</sup> Interface engineering must simultaneously passivate target defects while not creating additional defects in the subsequent layer that may hinder charge generation, extraction, or transport.<sup>19</sup>

All-back-contact (ABC) architectures that employ both electrodes on the same side of the absorber offer several potential benefits. First, they eliminate reflection and parasitic absorption associated with front contacts, which increases the amount of light that reaches the perovskite absorber and thus the maximum achievable current and efficiency.<sup>20</sup> Second, they remove the charge transport requirements from the

<sup>1</sup>National Renewable Energy Laboratory, Golden, CO 80401, USA

<sup>2</sup>Department Chemical and Biological Engineering, Colorado School of Mines, Golden, CO 80401, USA

<sup>3</sup>Department of Physics and Astronomy, Bowling Green State University, Bowling Green, OH 43403, USA

<sup>4</sup>Materials Science and Engineering Program, University of Colorado, Boulder, CO 80309, USA

<sup>5</sup>Lead contact

\*Correspondence: lance.wheeler@nrel.gov

<https://doi.org/10.1016/j.xcsp.2021.100363>



front interface, allowing a host of passivation and encapsulation strategies that do not require idealized charge transport to be employed.<sup>21,22</sup> Lastly, they open the door to unique *in situ* characterization techniques that probe the perovskite under device operation.<sup>23</sup> The ABC format is clearly promising, and the potential has been confirmed by the silicon community, in which ABC devices outperform their planar counterparts.<sup>24,25</sup>

ABC structures require feature sizes that are similar to, or shorter than, the diffusion length of free carriers within the absorber, necessitating photolithography or similar small-scale fabrication techniques. The performance of perovskite ABC devices are currently well short of their expected efficiencies due to challenges in producing micro-patterned electrodes with the proper geometry, electrode isolation, and quality interfaces with the perovskite absorber. A number of different architectures have been explored,<sup>26–29</sup> primarily spearheaded by Bach et al.<sup>30–35</sup> Notably, the quasi-interdigitated electrode architecture simplified processing to a single photolithography step while avoiding isolation defects associated with conventional interdigitated electrode processing.<sup>36</sup> The architecture was further improved by passivating the front surface to reach a state-of-the-art stabilized power output of 4.4%.<sup>22</sup>

In this work, we show that ABC devices are currently limited by defective interfaces, which arise from the unique challenge of having both the hole and electron transport layers simultaneously exposed during device fabrication. First, we highlight the critical role of complementary interface formation on ABC architectures and demonstrate methods to achieve devices with current-voltage scan PCE >10%. We then apply X-ray and ultraviolet photoelectron spectroscopy (XPS/UPS) to track the near-surface chemical composition of both contact interfaces ( $\text{NiO}_x$  and  $\text{TiO}_2$ ) and work function and valence band maximum spectra of  $\text{NiO}_x$  through the interface formation process. Finally, we use trends from the photoelectron spectroscopy measurements to inform a two-dimensional (2D) drift-diffusion model that illuminates how interface defect densities, energetic alignments, and injection barriers impact device performance, ultimately providing a pathway to >20% PCE using ABC architectures.

## RESULTS

### Overcoming ABC fabrication challenges and inherent coupling of ABC device interfaces

Three main challenges in ABC electrode fabrication include: (1) patterning the electrodes with resolution at scales less than, or equal to, the diffusion length of photo-generated carriers in the perovskite film; (2) achieving high shunt resistance between the two electrodes; and (3) maintaining optimum interfaces throughout formation. We overcome these three challenges by modifying an existing quasi-interdigitated electrodes ABC architecture.<sup>31</sup>

We achieved sufficiently small feature sizes using a photolithography process. Our devices feature a 7-μm pitch with 4.5-μm-diameter holes (Figures 1A–1C) in a honeycomb array (Figures 1D and S1). Polycrystalline perovskite thin films are commonly reported to have electron and hole diffusion lengths of ~1 μm,<sup>6</sup> which is the resolution limit of standard photolithography equipment.<sup>37</sup> Achieving this resolution can be challenging due to substrate imperfections. However, >12-μm diffusion lengths were demonstrated in similar ABC perovskite solar cells due to minority carriers being rapidly collected by the corresponding electrode below while majority carriers laterally diffuse in the perovskite layer.<sup>27</sup> An order of magnitude larger carrier diffusion length in an ABC device versus a bare film relaxes the patterning resolution requirements of ABC fabrication.

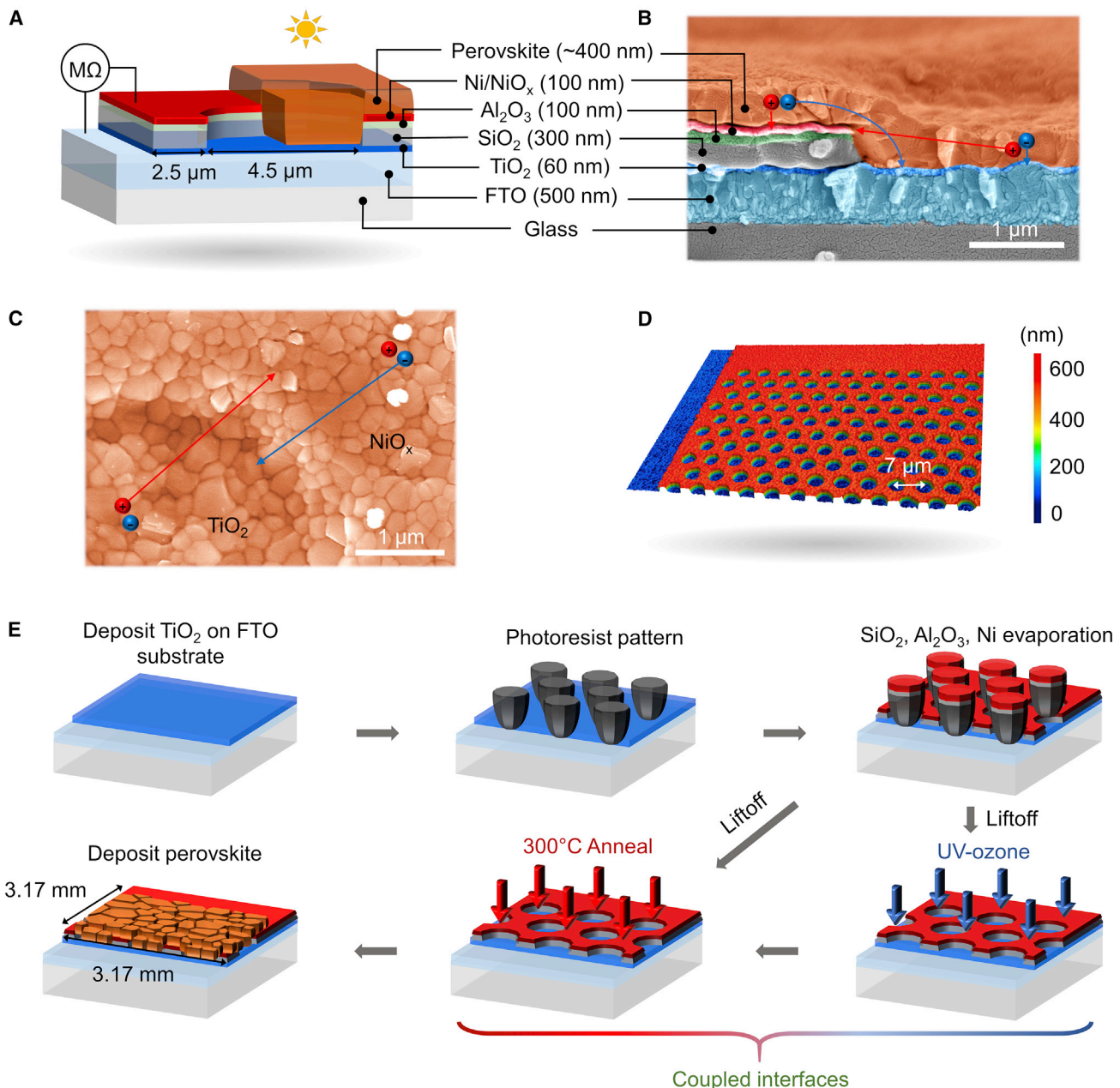


**Figure 1. Overcoming all-back-contact electrode fabrication challenges**

(A) Device schematic highlighting the electrode architecture and interfaces.

(B) False-colored cross-section scanning electron microscopy (SEM) image of a completed ABC device highlighting the dual dielectric and conformal perovskite layer.

(C) False-colored plan-view SEM image at the interface of the transport layers. Blue and red spheres illustrate extraction pathways for photogenerated electrons and holes, respectively.

(D) 3D profilometry image of the bare honeycomb quasi-interdigitated electrodes.

(E) Fabrication procedure highlighting the UV-ozone and 300°C anneal steps used to effectively prepare both surfaces to interface with the perovskite.

We obtained high shunt resistance by using a dual dielectric stack to electrically isolate the electrodes (Figures 1A and 1B). Single dielectric layers of alumina or silica of equivalent thickness provided only kΩ range resistance from two-point ohmmeter measurements (Table S1). Deposition of alumina sequentially over silica drastically

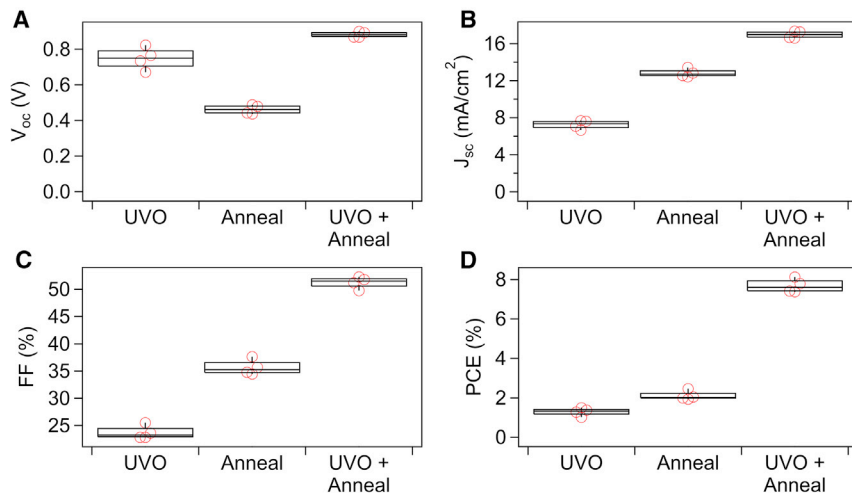


**Figure 2. Interface processing effects on ABC perovskite solar cell device performance**

Boxplots of reverse-scan device performance parameters from four devices utilizing each interface treatment. (A) Open-circuit voltage ( $V_{oc}$ ), (B) short-circuit current density ( $J_{sc}$ ), (C) fill factor (FF), and (D) power conversion efficiency (PCE) are shown. Box-plot quartiles were computed using Tukey method. ABC devices were exposed to UVO for 15 min and annealed for 45 min at 300°C.

increased the shunt resistance from the kΩ range to >1MΩ. Multilayer dielectric films have been known to mitigate pin-hole defects, create interfacial depletion layers, and increase breakdown voltage.<sup>38–40</sup> Optimized deposition parameters could also lead to compact and non-leaky single dielectric films, but we found the multi-layer deposition integral to achieving consistent electrode isolation.

We improve interfacial properties by developing a post-treatment process that has a synergistic effect on the coupled exposed interfaces. ABC fabrication presents a unique challenge compared to conventional planar devices because both the electron and hole transport layers are exposed before perovskite deposition (Figures 1D and 1E). Patterning limits transport layer choice because organic options are damaged during the photolithography processing. Therefore, oxide transport layers ( $\text{NiO}_x$  and  $\text{TiO}_2$ ) were used in this study. The  $\text{TiO}_2$  electron transport layer was deposited by a standard spin-coating and annealing procedure.<sup>41</sup> The nickel oxide ( $\text{NiO}_x$ ) hole transport layer was formed *in situ* by partial oxidation of the Ni metal contact through air annealing and/or UV-ozone (UVO) exposure after the patterning process (Figure 1E). These treatments also affect the  $\text{TiO}_2$  electron transport layer below due to the coupled interface nature of the ABC architecture (Figure 1E).

Metal oxide charge transport properties are controlled by defect chemistry and oxidation states that are tuned during the oxidation processes. Change in metal oxide properties caused by the different interface formation processes dramatically influences device performance (Figure 2). The annealing temperature of 300°C was chosen to provide comparison to other ABC device studies.<sup>22,27</sup> The 300°C annealing time was fixed to 45 min, by studying an analogous vertical device structure (Figure S2). UVO exposure time was fixed to 15 min to limit the number of independent variables. UVO treatment alone increased the open-circuit voltage ( $V_{oc}$ ) nearly 2-fold compared to the samples that were only annealed (Figure 2A) but resulted in reductions to short-circuit current density ( $J_{sc}$ ) and fill factor (FF) (Figures 2B and 2C). UVO exposure followed by annealing was synergistic for all parameters (Figures 2A–2D).

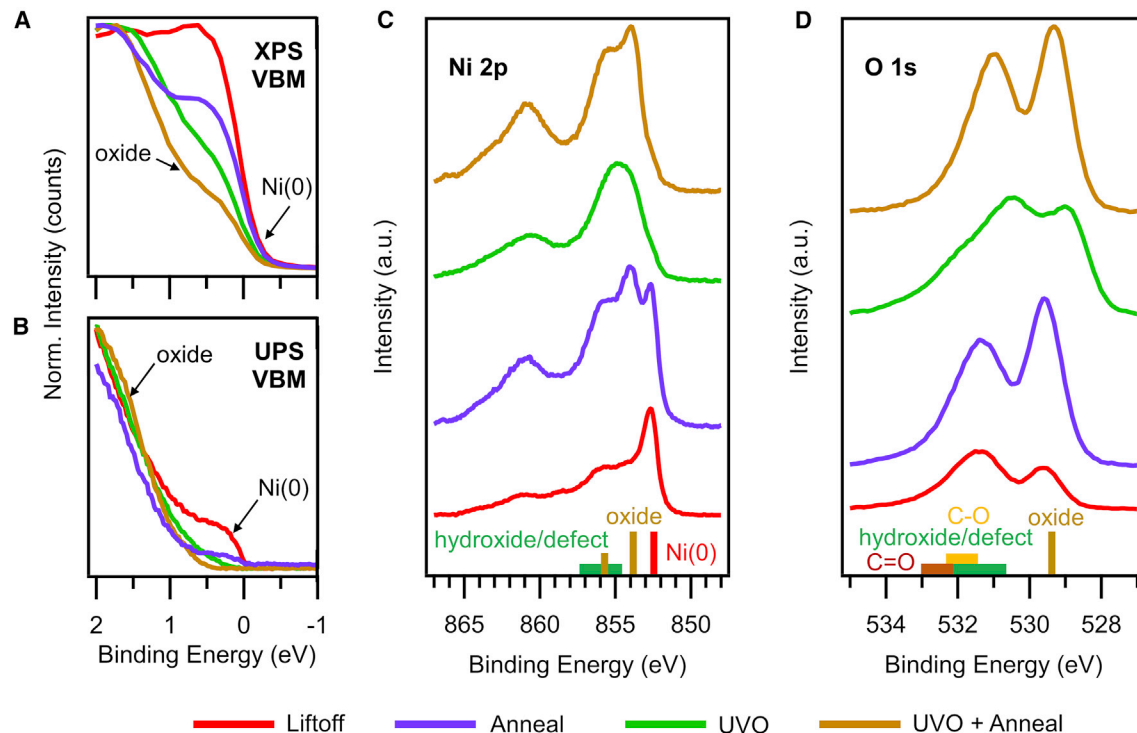


**Figure 3. Investigation of the Ni-NiO<sub>x</sub> surface through UV/O<sub>3</sub> exposure and annealing**

(A and B) XPS valence band maximum (VBM) spectra (A) and UPS VBM spectra (B) of the Ni-NiO<sub>x</sub> surfaces after liftoff (red), annealing at 300°C in air for 45 min (purple), UVO exposure for 15 min (green), and sequential 15-min UVO exposure followed by a 300°C anneal in air for 45 min (gold). (C and D) Corresponding XPS spectra of the Ni 2p core-levels (C) and O 1s core levels (D). XPS spectra are baseline subtracted and offset for clarity. Colored bars at the bottom of (C) and (D) indicate expected binding energies of relevant species.<sup>44,46,70,71</sup>

### Formation of the NiO<sub>x</sub> interface

The most sensitive process in our ABC fabrication is the formation of NiO<sub>x</sub> from metallic Ni. The layer must be pin-hole free, have a composition suitable for selective hole transport, and exhibit favorable energetic alignment with the valence band of the perovskite absorber. We form a compact, pin-hole-free NiO<sub>x</sub> layer with favorable transport properties by first exposing the Ni to UVO to form a clean, uniform seed layer and then annealing the film at 300°C.

We tracked the near-surface valence band spectra (Figures 3A and 3B) and chemical composition (Figures 3C, 3D, and S3) of the Ni-NiO<sub>x</sub> surfaces post-liftoff and after three interface formation processes using XPS and UPS to correlate the changes in device performance with material properties of the NiO<sub>x</sub> surface. Figure S3 shows the core levels, survey scan, and corresponding elemental composition; Figures 3A and 3B show the XPS and UPS valence band spectra, respectively; and Figures 3C and 3D show the relevant Ni 2p and O 1s core-level spectra for each of the samples. NiO<sub>x</sub> surface properties are highly complex and process dependent, with films presenting varied spectra/Gaussian envelopes that correspond to a mixture of Ni(II) (Ni<sup>2+</sup>), Ni(III) (Ni<sup>3+</sup>), and Ni(IV) (Ni<sup>4+</sup>) oxidation states.<sup>42,43</sup> Although obtaining quantitatively robust fits for NiO<sub>x</sub> is challenging due to the numerous and sometimes multiplet or asymmetric peaks formed by each of the oxidation states of Ni,<sup>44</sup> the relevant surface chemistry has been examined in the context of other PV technologies<sup>45</sup> and in traditional vertical p-i-n perovskite devices.<sup>46</sup>

Our analysis of the spectral envelopes of Ni 2p for all samples identified three different chemical states, listed from low to high binding energy, related to specific features in the spectra for each assignment, with markers included to guide the reader ([Figures 3C and 3D](#)): (1) Ni(0) or metallic Ni, which is from the evaporated nickel layer (~852.6 eV); (2) oxide or NiO, which has two characteristic peaks (~853.7 eV and ~855.7 eV),<sup>44,47</sup> and (3) hydroxide/defect, which could include Ni(OH)<sub>2</sub> (~855 eV), undercoordinated Ni defects in the NiO lattice, Ni<sub>2</sub>O<sub>3</sub>, γ-NiOOH (mixture of Ni(II) and Ni(IV)), and β-NiOOH (mixture of Ni(II), Ni(III), and Ni(IV)), with possible overlapping contributions from other species (~857 eV).<sup>45,46,48</sup> NiO, Ni(OH)<sub>2</sub>, and NiOOH are commonly observed in NiO<sub>x</sub> films.<sup>42,45</sup>

All samples have a metallic feature present at the Fermi edge in the XPS valence band maximum (VBM) ([Figure 3A](#)) and at ~852.6 eV in the Ni 2p core level spectrum ([Figure 3C](#)). This suggests we are selectively oxidizing the surface of the nickel layer and that metallic nickel exists at depths <10 nm for all samples, as confirmed by time-of-flight secondary ion mass spectrometry (ToF-SIMS) ([Figure S4](#)). However, the clear differences in the Ni 2p and O 1 s core-level spectra ([Figures 3C and 3D](#)) indicate we are changing the surface oxidation of the samples. Moreover, the UPS VBM measurements ([Figure 3B](#)), which have an information depth about a quarter of XPS, suggest that this change in oxidation results in drastically different electronic profiles near the surface.

Formation of a uniform NiO<sub>x</sub> layer over the metallic Ni(0) was critical for ABC device performance. The Ni surface was confirmed to be primarily metallic Ni(0) after liftoff and before exposure to UVO or annealing ([Figure 3C](#)). This metallic Ni(0) signature in the Ni 2p envelope correlates well with a metallic Ni(0) feature in the XPS and UPS VBM ([Figures 3A and 3B](#)), which have surface analysis depth of approximately ~8 nm and ~2 nm, respectively. A strong metallic Ni(0) contribution remains in all these features after the 300°C anneal. We believe that the presence of these Ni(0) signatures within the UPS analysis volume ([Figure 3B](#)) coupled with the equal depth of O in Ni evident from ToF-SIMS ([Figure S4](#)) indicates a non-uniform NiO<sub>x</sub> growth from the anneal process, leaving metallic Ni domains near the top 1 to 2 nm of the surface without UVO treatment. Metallic Ni in contact with the perovskite limits the achievable quasi-fermi level splitting and  $V_{OC}$  and is known to introduce deep trap levels creating nonradiative recombination centers.<sup>49</sup> The metallic Ni features present near the surface are consistent with ABC devices exhibiting significantly lower  $V_{OC}$ .

UVO exposure formed a more continuous NiO<sub>x</sub> film on metallic Ni and increased the work function to yield improvements in the  $V_{OC}$  of ABC devices. UPS VBM measurements ([Figure 3B](#)) and XPS Ni 2p core level ([Figure 3C](#)) confirmed the metallic Ni contribution was dramatically reduced after UVO exposure compared to the unexposed and only annealed samples. This reduction of metallic Ni(0) features in XPS correlates well with the elimination of the metallic Ni(0) feature in the UPS VBM, suggesting a conformal >2-nm-thick NiO<sub>x</sub> layer covers the surface of the nickel for samples exposed to UVO. The UVO treatment also increased the work function of the Ni-NiO<sub>x</sub> surface considerably ( $\Delta\phi$  ~0.65 eV) from the state immediately following liftoff ([Figure S5](#)). A conformal NiO<sub>x</sub> coverage and higher work function is commensurate with our observation of a drastic increase in  $V_{OC}$  in the UVO-treated samples.

Annealing at 300°C after UVO exposure caused the FF and  $J_{SC}$  of ABC devices to increase considerably.  $V_{OC}$  also increased by ~130 mV. We primarily attribute the increased performance to a change in the oxide to hydroxide/defect contributions. Exposing the post-liftoff films to UVO led to an increase in regions of the Ni 2p ([Figure 3C](#)) and O1s spectra

envelopes (Figure 3D) that correspond to hydroxide/defect contributions, which is consistent with other studies.<sup>50,51</sup> Subsequent annealing resulted in a spectral envelope for Ni 2p that closely resembles that of NiO; the spectrum has less hydroxide/defect contributions than the UVO-only sample and lacks the presence of Ni(0) that was observed in the anneal-only sample. We also see a general reduction in the ratio of Ni(0) to oxide features in the XPS VBM (Figure 3A), as well as a ~0.1-eV shift of the work function to lower binding energy (Figure S5). However, we note this small change in energetics may not be what is dominating device performance, as higher oxidation states of nickel have been shown to react with the perovskite. For example, Boyd et al.<sup>46</sup> found undercoordinated metal cation sites (Ni(III/IV) or Ni $\geq 3+$ ) react with dissociated lead halide and protonated amine precursors in perovskite solutions, causing perovskite A-site deficiencies or a Pb $l_{2-x}$ Br $_x$ -rich layer at the perovskite-NiO $_x$  interface. The Pb $l_{2-x}$ Br $_x$ -rich layer acts as an extraction barrier that limits  $V_{OC}$ . A thick Pb $l_{2-x}$ Br $_x$ -rich layer could also add series resistance to the device to lower FF and  $J_{SC}$ . The clear difference between the sample annealed after UVO exposure compared to the sample just exposed to UVO correlates well with ABC device performance and is consistent with literature. Additionally, trends in the ABC devices and photoelectron spectroscopy are overall consistent with analogous planar p-i-n devices investigated with the Ni/NiO $_x$  as the bottom contact (Figure S6).

#### Corresponding effects on the TiO<sub>2</sub> interface

The NiO $_x$  interface formation process simultaneously improved the TiO $_2$  contact. TiO $_2$  surfaces at the bottom of the holes in the patterned ABC bare electrodes are exposed to the same processes as the Ni-NiO $_x$  surfaces. We fabricated planar n-i-p devices to investigate the impacts of the photolithography and interface formation processes on the TiO $_2$  contact independent of the NiO $_x$  changes in an ABC device. Photoresist was spun onto TiO $_2$ , removed, and then devices were completed under varied conditions. UVO exposure to the TiO $_2$  increased the  $V_{OC}$  ~18% (Figure 4A), left the  $J_{SC}$  largely unchanged (Figure 4B), and increased FF ~32% (Figure 4C), leading to an ~60% enhancement in PCE (Figure 4D) compared to the liftoff state. The FF improvements are primarily due to lower series resistance rather than higher shunt resistance (Figure 4E). We note that, similar to the ABC devices, UVO exposure was required to achieve relatively high device performance after liftoff. UVO treatment has previously been shown to enhance TiO $_2$ -perovskite interfaces by removing surface carbon contaminants, improving wettability, and increasing conductivity.<sup>52–54</sup>

XPS was used to track the near-surface chemical environment of the TiO $_2$  surfaces on the ABC devices after liftoff and through each fabrication step. Ti 2p and O 1 s core levels remained largely unchanged, suggesting that a change in TiO $_x$  oxidation states did not dominate device performance (Figure S7). However, the carbon content in each sample varied significantly (Figure S7). Removing residual carbon species from the photolithography process was paramount (Figure 4F). The overall C:Ti ratio reduced significantly immediately after UVO exposure but increased after the anneal process in air due to adventitious carbon (Figure 4F). However, a unique high binding energy feature was only present on the TiO $_2$  surfaces not subject to UVO (Figures 4F and S8). We attribute the high binding energy feature to be a shake-up satellite due to  $\pi$ - $\pi^*$  electron transitions in the aromatic species in the residual photoresist.<sup>55</sup> Removing the residual photoresist coincides with increase in FF,  $V_{OC}$ , and PCE. Overall, UVO exposure was a complementary interface formation process for both the TiO $_2$  and NiO $_x$  contacts.

#### 2D device modeling

Current density-voltage (JV) curves of ABC devices have a number of unique features, depending on interface process conditions: (1) pronounced roll-over of the

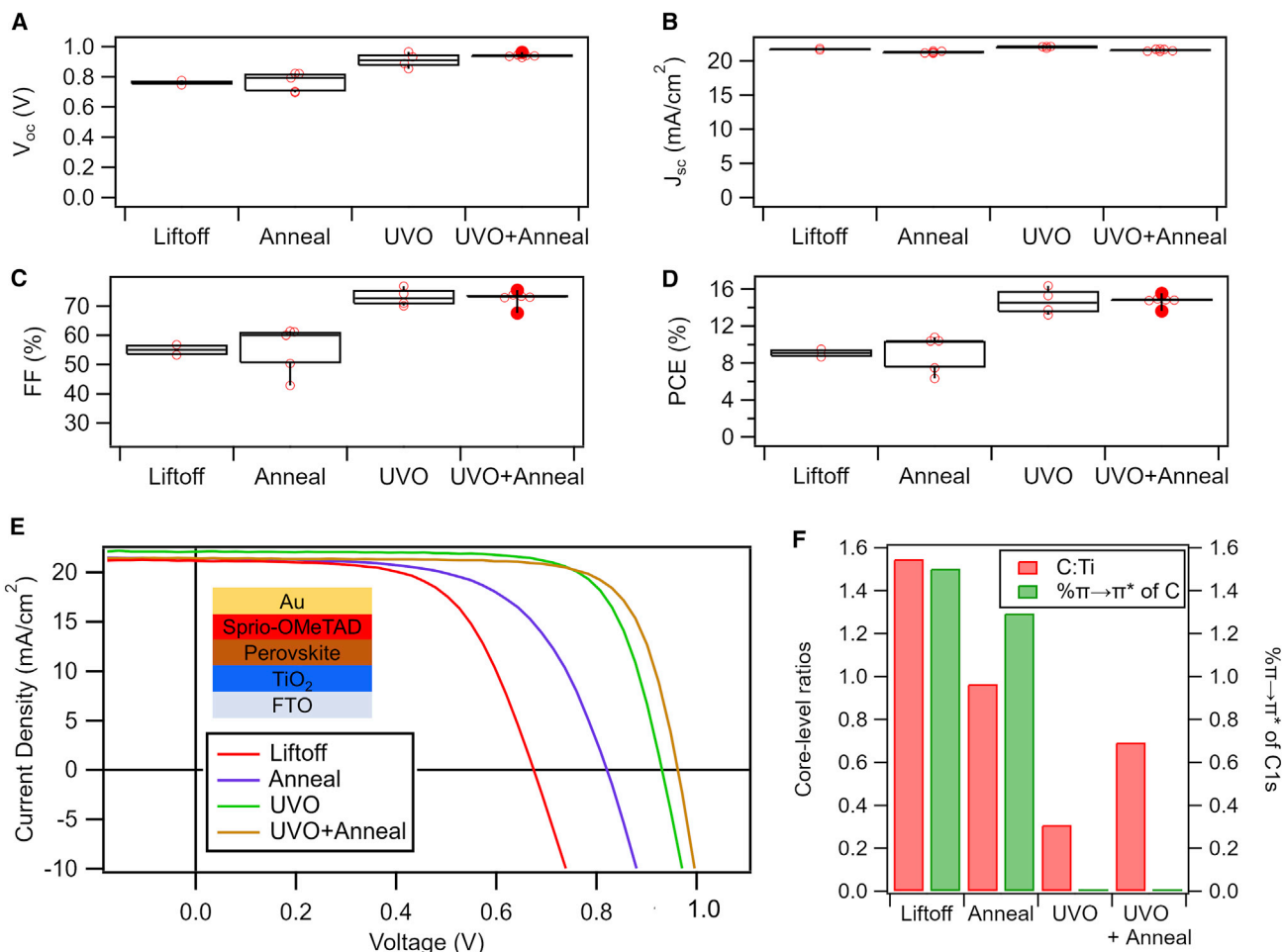


**Figure 4. Analogous planar n-i-p TiO<sub>2</sub> devices to study impacts of interface processing**

(A–D) Summary of reverse-scan solar cell performance metrics for the planar n-i-p devices, including  $V_{OC}$  (A),  $J_{SC}$  (B), FF (C), and PCE (D). Filled-in circles are outliers based on the Tukey quartile method.

(E and F) Representative reverse-scan JV curves (E) for the TiO<sub>2</sub> surfaces subjected to the photolithography process and each post-processing condition (F) C 1 s:Ti 2p core-level ratios and  $\pi \rightarrow \pi^*$ % of the C 1 s peak.

curves under forward bias; (2) significant increase in  $V_{OC}$  for the contacts with UV/O treatment compared to annealing only; and (3) reduced  $J_{SC}$  and high series resistance for the contacts only exposed to UV/O (Figure 5A). We employed two-dimensional (2D) device modeling to investigate the origin of these JV features based on interface properties inferred from the XPS/UPS analysis. The semiconductor transport equations were solved in a 2D, axially symmetric domain to account for both lateral and transverse charge transport.<sup>20,56–59</sup> Details, including device dimensions, parameter definitions, and material values from literature, are provided in Note S1. Major assumptions of the model were (1) all device models had an ohmic TiO<sub>2</sub> contact (Figures S9 and S10); (2) model for devices only exposed to annealing did not include a NiO<sub>x</sub> layer above the Ni contact, inferred from the XPS/UPS data; and (3) model for devices exposed to UV/O had a 10-nm-thick NiO<sub>x</sub> layer. ToF-SIMS analysis revealed the NiO<sub>x</sub> is between 5 and 10 nm thick (Figure S4).

We studied the effects of pertinent interface variables within a reasonable range of values. Contact work functions, electron affinities (band alignments), interface defect

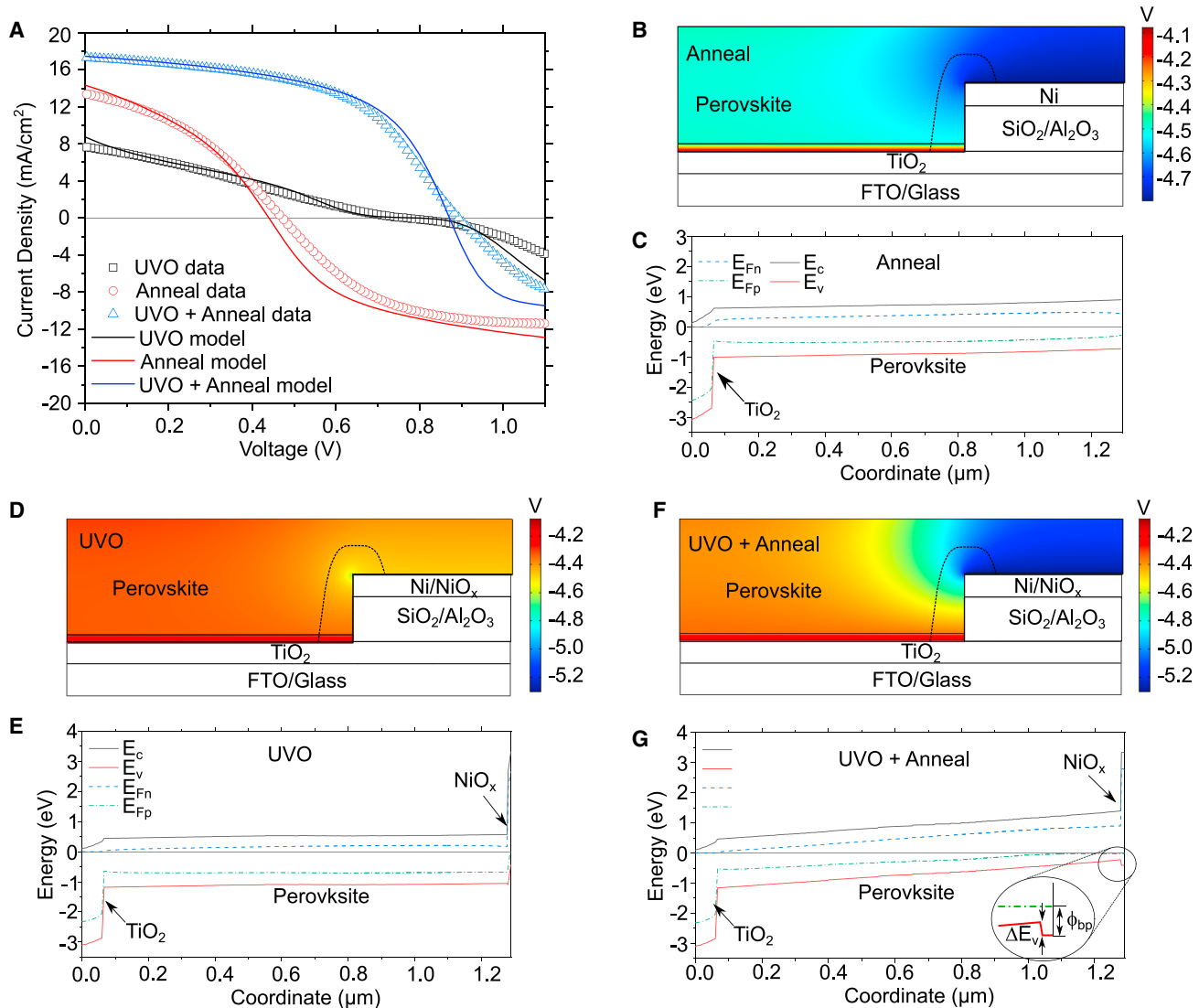


**Figure 5. Insights into JV characteristics via 2D drift-diffusion modeling**

(A) Modeled JV curves plotted against experimental data.

(B–G) 2D potential maps and 1D energy band diagrams along the corresponding curved dashed line of each model for devices subject to (B and C) 300°C annealing process, (D and E) UVÖ exposure, and (F and G) UVÖ followed by the 300°C annealing process. The main parameters differentiating each model are summarized in Table 1.

densities, and front (illuminated) surface recombination velocity were considered (Note S2). A minimal number of independent variables were determined to describe the three JV curve types (Figure 5A) while qualitatively corresponding with the trends observed by XPS/UPS. Three key variables (Table 1) were identified: (1) Ni work function ( $\phi_{Ni}$ ); (2) interface defect density at the perovskite/ $\text{NiO}_x$  interface ( $N_{i,NiO_x}$ ); and (3) interface defect density at the perovskite/ $\text{TiO}_2$  interface ( $N_{i,TiO_2}$ ). JV simulations (Figure 5A) suggest that  $\phi_{Ni}$  increased with UVÖ treatment, thereby improving  $V_{OC}$  and reducing JV curve roll-over. UVÖ treatment also decreased  $N_{i,TiO_2}$ , providing minor improvements to  $V_{OC}$  and  $J_{SC}$ .

JV roll-over is often associated with a barrier to majority carrier injection.<sup>60,61</sup> For models with the  $\text{NiO}_x$  layer, the barrier height,  $\phi_{bp}$ , depended on the work function

**Table 1. Key model parameters**

|              | $N_{i,\text{NiO}_x} (\text{cm}^{-2})$ | $N_{i,\text{TiO}_2} (\text{cm}^{-2})$ | $\phi_{\text{Ni}} (\text{eV})$ |
|--------------|---------------------------------------|---------------------------------------|--------------------------------|
| Anneal       | N/A                                   | $1.5 \times 10^{12}$ (acceptors)      | 4.8                            |
| UVO          | $5 \times 10^{12}$ (donors)           | $1 \times 10^{12}$ (acceptors)        | 5.3                            |
| UVO + anneal | $1 \times 10^{10}$ (donors)           | $1 \times 10^{12}$ (acceptors)        | 5.3                            |

at the Ni contact,  $\phi_{\text{Ni}}$ ; the  $\text{NiO}_x$  band gap,  $E_{g,\text{NiO}}$ ; and the  $\text{NiO}_x$  electron affinity,  $\chi_{\text{NiO}}$ , according to  $\phi_{bp} = \chi_{\text{NiO}} + E_{g,\text{NiO}} - \phi_{\text{Ni}}$ . Models for devices that were only annealed did not include the  $\text{NiO}_x$  layer. In those cases, the hole injection barrier was  $\phi_{bp} = \chi_p + E_{g,p} - \phi_{\text{Ni}}$ , where  $\chi_p$  and  $E_{g,p}$  are the electron affinity and band gap of the perovskite, respectively. Without the  $\text{NiO}_x$  layer, a value of  $\phi_{\text{Ni}} = 4.8$  eV ( $\phi_{bp} = 0.72$  eV) represented the JV curve roll-over of the device subjected only to annealing (Figure 5A). For models with the  $\text{NiO}_x$  layer, a value of  $\phi_{\text{Ni}} = 5.3$  eV ( $\phi_{bp} = 0.41$  eV) was representative. An increase in Ni work function with UVO exposure is qualitatively consistent with UPS data (Figure S5) and accounts for most of the observed  $V_{OC}$  increase.

When interface defect densities are sufficiently high, relative to the doping of the contact layers, their charge states have a more dominant effect on the electric field and device performance than interface recombination alone (Figure S12). The effects are visualized using 2D potential maps and 1D energy band diagrams. The potential gradients in the anneal-only model (Figures 5B and 5C) indicate a lower electric field than the UVO-only model (Figures 5D and 5E), due to the positively charged defects at the perovskite/ $\text{NiO}_x$  interface. The positively charged defects hinder carrier collection. However, the overall potential difference is greater in the UVO-only device due to the higher Ni work function, resulting in higher  $V_{OC}$ . Devices that were exposed to UVO and then annealed had the largest potential drop across the perovskite due to the high Ni work function and a reduction in defect density by two orders of magnitude at the perovskite/ $\text{NiO}_x$  interface (Table 1) to yield increased  $J_{SC}$  and FF (Figures 5F and 5G). A minor improvement in  $V_{OC}$  and  $J_{SC}$  was established by slightly decreasing the interface defect density at the perovskite/ $\text{TiO}_2$  interface relative to the device that was not UVO treated, reminiscent to a less-defective interface due to removal of residual carbon species. Sufficient mitigation of charged defects at the interfaces creates a *de facto* p-i-n solar cell structure with a strong electric field maintained across the full perovskite absorber that enhances carrier collection efficiency (Figures 5F and 5G).

Though we do not define the chemical identity of the charged defects in our model, they may either be fixed defect states at the interfaces or mobile ions in the perovskite film that migrate toward the interfaces and screen the electric field, generating a similar flat band condition within the bulk of the perovskite film.<sup>62</sup> Studying those possibilities with time dependence and hysteresis effects are beyond the present scope. The flat band condition due to charged defects is largely responsible for the low  $J_{SC}$  and FF, but it is possible that a small extraction barrier or valence band offset between the perovskite and  $\text{NiO}_x$ , shown to be 0.19 eV in the inset of Figure 5G, provided some additional  $J_{SC}$  limitation. The offset may represent a  $\text{PbI}_{2-x}\text{Br}_x$ -rich layer formed as a result of the reaction between  $\text{Ni}^{\geq 3+}$  defects and perovskite precursors, as previously observed.<sup>46</sup>

Surface recombination velocities were estimated from the interface defect densities in general as  $S = N_i \sigma v_{th}$ , where  $\sigma$  is the capture cross-section and  $v_{th}$  is the thermal velocity.<sup>63</sup> In these models, both electrons and holes had values of  $\sigma = 10^{-14} \text{ cm}^2$

and  $v_{th} = 10^7$  cm/s, respectively. The values in [Table 1](#) indicate a range of  $S = 10^3$  to  $5 \times 10^5$  cm/s at the perovskite/oxide interfaces. Front surface recombination,  $S_{fs}$ , was set to  $10^4$  cm/s for these models based on our sensitivity analysis ([Figure S11](#)). These values are much larger than the best reported values for perovskite materials ( $S \sim 1$  cm/s).<sup>27</sup>

### Pathway to >20% PCE for ABC perovskite solar cells

ABC devices have been modeled in previous work by Yang et al.<sup>56</sup> to achieve PCE < 25% with reasonable values of carrier lifetimes, mobilities, interface defect densities, surface recombination velocity, and pitch spacing. They also demonstrated PCE > 29% could be realized in ABC devices with advanced optical management.<sup>56</sup> ABC devices were most notably shown to outperform planar perovskite devices over a wide range of parameters. Here, we extended our simulations to study how to improve our modeled ABC devices through interface engineering. We assumed a more-conservative carrier lifetime of 192 ns ([Table S2](#)) and reflectivity of 5%, whereas Yang et al. assumed 2,730 ns and 2.5%.

Our experimental work shows there is significant room for improving ABC devices to reach their theoretical potential. First, we recognize the work function of the hole contact must be increased from 5.3 eV to 5.5 eV to achieve >20% devices. Assuming proper band alignment at the hole contact, we calculate ABC device performance metrics by applying the device model described above to determine the critical values of  $S_{fs}$  and interface defect density for improving performance ([Figure 6](#)).

Interface defect densities less than  $2 \times 10^{11}$  cm<sup>-2</sup> are paramount for realizing ABC devices with >20% PCE ([Figure 6A](#)). With favorable interface conditions,  $S_{fs} < 200$  cm/s is then required. Increasing  $V_{OC}$  beyond the 1.0 V shown in our experimental work is strongly dependent on interface defect density ([Figure 6B](#)), whereas  $J_{SC}$  and FF are more dependent on  $S_{fs}$  when interface defect densities are below  $10^{11}$  cm<sup>-2</sup> ([Figures 6C and 6D](#)). Our experimental devices need at least a two-order-of-magnitude improvement in interface defect density and  $S_{fs}$ .

The front surface of the perovskite absorber is the only interface we have yet to consider experimentally. We targeted reduced  $S_{fs}$  by limiting solvent vapor concentration during perovskite deposition and by applying a poly(methyl methacrylate) (PMMA) coating to our exposed perovskite surface ([Figure 7A](#)). Concentration of solvent vapor is well known to impact perovskite crystallization to yield significant changes in grain size, uniformity, and surface passivation.<sup>64–66</sup> PMMA coatings are known to chemically passivate the front surface of the perovskite and acts as an anti-reflection coating.<sup>22,27</sup> We observe an increase in  $J_{SC}$  from reduced front-surface reflection and an increase in  $V_{OC}$  and FF after reducing the solvent vapor concentration during spin coating and applying a PMMA layer ([Figures 7B and S13](#)).

Tailoring the front surface and crystallization conditions yields a champion ABC device with 11.2% reverse-scan PCE and 9.79% forward-scan PCE (10.5%  $\pm$  0.7% average forward and reverse scan PCE). However, JV hysteresis ([Figure 7B](#)) and mismatch between JV scan efficiencies and stabilized power output are significant. The power output decreases to <3% PCE and does not fully stabilize after 25 min under constant illumination and forward bias ([Figure S14](#)). The discrepancy between the power output over time at a fixed voltage versus the JV scan PCE is likely linked to unstable interfacial species at maximum power point conditions. Accordingly, the higher initial JV performance from the devices exposed to UVO and then annealed may be due to increased metastable charged interfacial species, but it is difficult to

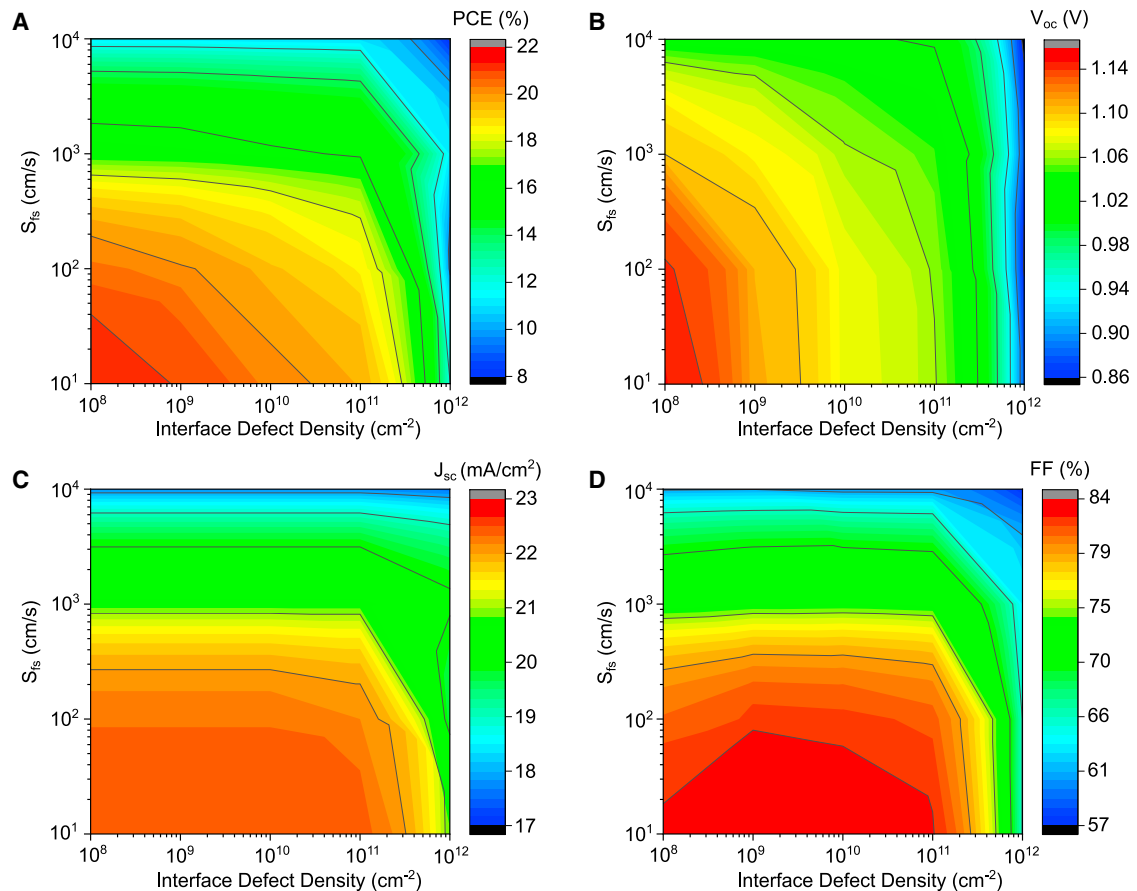


**Figure 6. Pathway to >20% efficiency for ABC perovskite solar cells**

Extending 2D device modeling to understand how to improve the ABC perovskite solar cells past 20% PCE. (A) PCE, (B)  $V_{oc}$ , (C)  $J_{sc}$ , and (D) FF as a function of  $S_{fs}$  and interface defect density. The work function was set to  $\phi_{Ni} = 5.5$  eV to avoid a majority carrier injection barrier. Defect densities were set equal at the  $\text{NiO}_x/\text{perovskite}$  and  $\text{TiO}_2/\text{perovskite}$  interfaces.

fully explain based on our current data. Weber et al.<sup>67</sup> found the formation and release of interfacial charges is the dominating factor for JV hysteresis.

## DISCUSSION

Our work highlights the importance of complementary interface processing in ABC perovskite solar cell architectures and presents an effective way to beneficially prepare both surfaces to interface with perovskite materials. For this  $\text{TiO}_2\text{-NiO}_x$  coupled interface system, a UV-ozone treatment was critical to simultaneously form a homogeneous  $\text{NiO}_x$  layer from the metallic Ni electrode and remove residual carbon species on the  $\text{TiO}_2$  electrode that were present from the photolithography patterning process. Subsequent annealing was necessary to increase the NiO content during conversion from  $\text{Ni}(0)$ . The dramatic evolution in JV behavior throughout ABC fabrication was captured by a 2D drift-diffusion model. Our model validates the trends observed in JV scan device performance and interface characterization and provides a roadmap for >20% ABC devices by identifying the critical metrics that must be met in future ABC device work: (1) increase the work function of the hole contact; (2) further reduce charged interface defect density; and (3) reduce the front surface recombination velocity below 100  $\text{cm/s}$ .

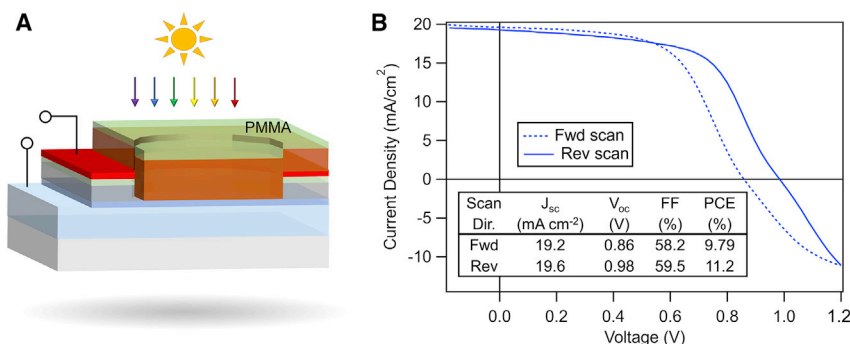


**Figure 7. Post-electrode processing manipulation of perovskite absorber**

Manipulating the front surface and perovskite crystallization process increased device performance.

(A) Device schematic with added poly(methyl methacrylate) (PMMA) front-surface coating.  
(B) Forward and reverse JV scans and solar cell metrics of champion device with lower solvent vapor concentration during perovskite deposition and front PMMA coating.

## EXPERIMENTAL PROCEDURES

### Resource availability

#### Lead contact

Further information and requests for resources and materials should be directed to and will be fulfilled by the lead contact, Lance M. Wheeler ([lance.wheeler@nrel.gov](mailto:lance.wheeler@nrel.gov)).

#### Materials availability

This study did not generate new unique materials.

#### Data and code availability

The published article includes all data analyzed and necessary to draw the conclusions of this study in the figures and tables of the main text and [Supplemental information](#). Further information and requests for further data should be directed to the lead contact.

### Substrate preparation

1" × 1" × 1.1 mm fluorine-doped-tin-oxide (FTO) patterned substrates were purchased from Thin Film Devices. The substrates were submerged and sonicated for 15 min sequentially in Liquinox diluted in deionized (DI) water, neat DI water, acetone, and isopropyl alcohol, followed by 15 min of UV-ozone from a commercial UVO cleaner (Jelight 342).

### Spin-coated TiO<sub>2</sub> electron transport layer

Titanium diisopropoxide bis(acetylacetone) solution was purchased from Sigma-Aldrich (75 wt % in isopropanol) and diluted in 2-butanol (Aldrich; 99%) to make a 0.2 M TiO<sub>2</sub>-precursor solution. 180 μL was dispensed onto the patterned FTO substrates and spun at 2,000 rpm for 30 s, and the films were annealed at 500°C for 1 h.

### ABC photolithography patterning

AZ-5214E photoresist was purchased from Integrated Micro Materials. The resist was spun at 4,000 rpm for 30 s, soft baked at 110°C for 1.5 min, exposed for 1.2 s with a standard i-g-h line UV-light source from ABM-USA, reverse baked at 114°C for 1.5 min, and developed in AZ-300 MIF developer for 23 s to create an optimal liftoff profile.

**SiO<sub>2</sub>, Al<sub>2</sub>O<sub>3</sub>, Ni electron-beam evaporation, and liftoff**

300 nm of SiO<sub>2</sub> was deposited at 5 Å/s 300 mA, followed by 100 nm of Al<sub>2</sub>O<sub>3</sub> at 2 Å/s 300 mA and 100 nm of Ni at 5 Å/s 600 mA. This stack was lifted in Remover-PG for 20 min stagnant and 2 min with sonication.

**Interface processing**

Samples were subject to UV-ozone treatment by placing samples <1 cm from a UV lamp of a commercial UVO cleaner (Jelight 342) operated in air. Samples were annealed in air using a Fisher Scientific Isotemp Muffle Furnace, model 550-14 at 300°C for 45 min.

**Perovskite deposition**

Triple-cation double-halide perovskite films of the form FA<sub>x</sub>MA<sub>y</sub>Cs<sub>1-x-y</sub>Pb(I<sub>z</sub>Br<sub>1-z</sub>)<sub>3</sub> were formed following a reported method.<sup>68</sup> Briefly, 22.4 mg MABr, 73.4 mg PbBr<sub>2</sub>, 172 mg FAI, 507 mg Pbl<sub>2</sub>, (0.2:0.2:1:1.1 mole ratio), and 40 µL of CsI stock solution (1.5 M in DMSO) were dissolved in 1 mL of 4:1 DMF:DMSO to form the perovskite precursor solution. Samples were transferred into a glovebox, and 50 µL of solution was deposited onto the patterned substrate and spun at 2,000 rpm for 10 s and 6,000 rpm for 20 s. During the spin process, 120 µL of chlorobenzene was dispensed onto the spinning substrate with 8 to 9 s remaining. Samples were annealed at 100°C for 1 h. Solvent vapor concentration present during deposition was limited by removing the lid of the spin coater for the results in Figure 7.

**Device testing**

JV measurements were performed in a nitrogen glovebox at room temperature using a Newport Oriel 94043A Sol3A Class AAA solar simulator that was calibrated each time before use with a silicon photodiode with a KG2 filter to 1-sun intensity. Scan speeds are 0.82 V/s with a dwell time of 0.01 s. All devices were light soaked for 5 min not under bias. All devices in this study have an unmasked active area of 0.10 cm<sup>2</sup>. For the champion device, masked areas were 0.06 cm<sup>2</sup>.

**Photoelectron spectroscopy methods**

Measurements were performed on a Physical Electronics 5600 photoelectron spectrometer, which has been discussed in detail previously.<sup>69</sup> Briefly, XPS radiation was produced by a monochromatic 350 W Al K $\alpha$  excitation centered at 1,486.7 eV. UPS radiation was generated by a He-gas discharge lamp (He I = 21.22 eV). All XPS core-level spectra were collected using a step size of 0.1 eV and pass energy of 23.50 eV although UPS spectra and XPS work function measurements were conducted with a step size of 0.025 and pass energy of 2.95 eV. The electron binding energy scale was calibrated using the Fermi edge and core levels of gold and copper substrates, cleaned with argon ion bombardment. UPS spectra were numerically corrected for satellite peaks that arise from the polychromic He I radiation. Work functions were determined using the intersection between the baseline and a linear fit to the main feature. VBMs were calculated using linear extrapolation of the main feature in the valence band region to the background signal. Spectra taken with the Al source are typically assigned an uncertainty of 0.05 eV. Compositional analyses and deconvolutions are typically assigned an uncertainty of 5%. See also [Supplemental experimental procedures](#).

**SUPPLEMENTAL INFORMATION**

Supplemental Information can be found online at <https://doi.org/10.1016/j.xcsp.2021.100363>.

## ACKNOWLEDGMENTS

This study was authored by the National Renewable Energy Laboratory, operated by Alliance for Sustainable Energy, for the US Department of Energy (DOE) under contract no. DE-AC36-08GO28308. K.J.P., M.M., E.L.W., D.T.M., C.A.W., and L.M.W. acknowledge funding from the Building Technologies Office within the US Department of Energy Office of Energy Efficiency and Renewable Energy. Contributions from S.P.D. and J.J.B. were supported by US Department of Energy's Office of Energy Efficiency and Renewable Energy under the Solar Energy Technologies Office (SETO) project "De-risking Halide Perovskite Solar Cells" program (DE-FOA-0000990). ToF-SIMS material makes use of the ToF-SIMS system at the Colorado School of Mines, which was supported by the National Science Foundation under grant no. 1726898. The authors thank Karen Bowers, a newly retired research technician at NREL, for running electron-beam evaporation for the dielectric and Ni stack; Max Hörantner for his initial insight into all-back-contact perovskite solar cells from his prior experience; Rosemary Bramante for running indium-doped zinc oxide sputter depositions for the planar p-i-n devices; and all the experienced perovskite solar cell scientists at NREL, including Caleb Boyd, Jérémie Werner, Severin Haberreutinger, Giles Eperon, and Taylor Moot for providing day-to-day laboratory insights. One or more of the authors of this paper self-identifies as an underrepresented ethnic minority in science. The author list of this paper includes contributors from the location where the research was conducted who participated in the data collection, design, analysis, and/or interpretation of the work.

## AUTHOR CONTRIBUTIONS

Conceptualization, K.J.P., C.A.W., and L.M.W.; methodology, K.J.P., M.N., S.P.D., G.T., C.A.W., and L.M.W.; formal analysis, K.J.P., M.N., S.P.D., J.J.B., and G.T.; investigation, K.J.P., S.P.D., G.T., and M.M.; writing – original draft, K.J.P., M.N., S.P.D., C.A.W., and L.M.W.; writing – review and editing, K.J.P., M.N., S.P.D., G.T., E.L.W., D.T.M., J.J.B., C.A.W., and L.M.W.; visualization, K.J.P., M.N., S.P.D., and G.T.; supervision, C.A.W., J.J.B., and L.M.W.

## DECLARATION OF INTERESTS

The authors declare no competing interests.

Received: August 13, 2020

Revised: February 3, 2021

Accepted: February 18, 2021

Published: March 12, 2021

## REFERENCES

1. Sun, S., Salim, T., Mathews, N., Duchamp, M., Boothroyd, C., Xing, G., Sum, T.C., and Lam, Y.M. (2014). The origin of high efficiency in low-temperature solution-processable bilayer organometal halide hybrid solar cells. *Energy Environ. Sci.* 7, 399–407.
2. De Wolf, S., Holovsky, J., Moon, S.J., Löper, P., Niesen, B., Ledinsky, M., Haug, F.J., Yum, J.H., and Ballif, C. (2014). Organometallic halide perovskites: sharp optical absorption edge and its relation to photovoltaic performance. *J. Phys. Chem. Lett.* 5, 1035–1039.
3. Wehrenfennig, C., Liu, M., Snaith, H.J., Johnston, M.B., and Herz, L.M. (2014). Homogeneous emission line broadening in the organo lead halide perovskite  $\text{CH}_3\text{NH}_3\text{PbI}_3_{x}\text{Cl}_{x}$ . *J. Phys. Chem. Lett.* 5, 1300–1306.
4. Wehrenfennig, C., Eperon, G.E., Johnston, M.B., Snaith, H.J., and Herz, L.M. (2014). High charge carrier mobilities and lifetimes in organolead trihalide perovskites. *Adv. Mater.* 26, 1584–1589.
5. Xing, G., Mathews, N., Sun, S., Lim, S.S., Lam, Y.M., Grätzel, M., Mhaisalkar, S., and Sum, T.C. (2013). Long-range balanced electron- and hole-transport lengths in organic-inorganic  $\text{CH}_3\text{NH}_3\text{PbI}_3$ . *Science* 342, 344–347.
6. Stranks, S.D., Eperon, G.E., Grancini, G., Menelaou, C., Alcocer, M.J.P., Leijtens, T., Herz, L.M., Petrozza, A., and Snaith, H.J. (2013). Electron-hole diffusion lengths exceeding 1 micrometer in an organometal trihalide perovskite absorber. *Science* 342, 341–344.
7. Johnston, M.B., and Herz, L.M. (2016). Hybrid perovskites for photovoltaics: charge-carrier recombination, diffusion, and radiative efficiencies. *Acc. Chem. Res.* 49, 146–154.
8. Pazos-Outón, L.M., Szumilo, M., Lamboll, R., Richter, J.M., Crespo-Quesada, M., Abd-Jalebi, M., Beeson, H.J., Vrućinić, M., Alsari, M., Snaith, H.J., et al. (2016). Photon recycling in lead iodide perovskite solar cells. *Science* 351, 1430–1433.
9. Cai, M., Wu, Y., Chen, H., Yang, X., Qiang, Y., and Han, L. (2016). Cost-performance analysis of perovskite solar modules. *Adv. Sci. (Weinh.)* 4, 1600269.
10. Xiao, Z., Kerner, R.A., Zhao, L., Tran, N.L., Lee, K.M., Koh, T.-W., Scholes, G.D., and Rand, B.P.

- (2017). Efficient perovskite light-emitting diodes featuring nanometre-sized crystallites. *Nat. Photonics* 11, 108–115.
11. Sutherland, B.R., and Sargent, E.H. (2016). Perovskite photonic sources. *Nat. Photonics* 10, 295–302.
  12. Yakunin, S., Sytnyk, M., Kriegner, D., Shrestha, S., Richter, M., Matt, G.J., Azimi, H., Brabec, C.J., Stangl, J., Kovalenko, M.V., and Heiss, W. (2015). Detection of X-ray photons by solution-processed organic-inorganic perovskites. *Nat. Photonics* 9, 444–449.
  13. Ma, F., Zhu, Y., Xu, Z., Liu, Y., Zheng, X., Ju, S., Li, Q., Ni, Z., Hu, H., Chai, Y., et al. (2020). Optoelectronic perovskite synapses for neuromorphic computing. *Adv. Funct. Mater.* 30, 1908901.
  14. Wheeler, L.M., Moore, D.T., Ihly, R., Stanton, N.J., Miller, E.M., Tenent, R.C., Blackburn, J.L., and Neale, N.R. (2017). Switchable photovoltaic windows enabled by reversible photothermal complex dissociation from methylammonium lead iodide. *Nat. Commun.* 8, 1722.
  15. Wheeler, L.M., and Wheeler, V.M. (2019). Detailed balance analysis of photovoltaic windows. *ACS Energy Lett.* 4, 2130–2136.
  16. NREL (2020). Cell efficiency chart. <https://www.nrel.gov/pv/cell-efficiency.html>.
  17. Shao, S., and Loi, M.A. (2020). The role of the interfaces in perovskite solar cells. *Adv. Mater. Interfaces* 7, 1901469.
  18. Christians, J.A., Schulz, P., Tinkham, J.S., Schloemer, T.H., Harvey, S.P., Tremolet de Villers, B.J., Sellinger, A., Berry, J.J., and Luther, J.M. (2018). Tailored interfaces of unencapsulated perovskite solar cells for >1,000 hour operational stability. *Nat. Energy* 3, 68–74.
  19. Schulz, P., Cahen, D., and Kahn, A. (2019). Halide perovskites: is it all about the interfaces? *Chem. Rev.* 119, 3349–3417.
  20. Yang, W., Yang, Z., Shou, C., Sheng, J., Yan, B., and Ye, J. (2020). Optical design and optimization for back-contact perovskite solar cells. *Sol. Energy* 201, 84–91.
  21. deQuilettes, D.W., Koch, S., Burke, S., Paranjpy, R.K., Shropshire, A.J., Ziffer, M.E., and Ginger, D.S. (2016). Photoluminescence lifetimes exceeding 8 μs and quantum yields exceeding 30% in hybrid perovskite thin films by ligand passivation. *ACS Energy Lett.* 1, 438–444.
  22. Bacal, D.M., Lal, N.N., Jumabekov, A.N., Hou, Q., Hu, Y., Lu, J., Chesman, A.S.R., and Bach, U. (2020). Solution-processed antireflective coating for back-contact perovskite solar cells. *Opt. Express* 28, 12650–12660.
  23. Alsari, M., Bikondoa, O., Bishop, J., Abd-Jalebi, M., Ozer, L.Y., Hampton, M., Thompson, P., Hörrantner, M.T., Mahesh, S., Greenland, C., et al. (2018). *In situ* simultaneous photovoltaic and structural evolution of perovskite solar cells during film formation. *Energy Environ. Sci.* 11, 383–393.
  24. Yoshikawa, K., Kawasaki, H., Yoshida, W., Irie, T., Konishi, K., Nakano, K., Uto, T., Adachi, D., Kanematsu, M., Uzu, H., et al. (2017). Silicon heterojunction solar cell with interdigitated back contacts for a photoconversion efficiency over 26%. *Nat. Energy* 2, 17032.
  25. Yamamoto, K., Yoshikawa, K., Uzu, H., and Adachi, D. (2018). High-efficiency heterojunction crystalline Si solar cells. *Jpn. J. Appl. Phys.* 57, 08RB20.
  26. Wong-Stringer, M., Routledge, T.J., McArdle, T., Wood, C.J., Game, O.S., Smith, J.A., Bishop, J.E., Vaenas, N., Coles, D.M., Buckley, A.R., et al. (2019). A flexible back-contact perovskite solar micro-module. *Energy Environ. Sci.* 12, 1928–1937.
  27. Tainter, G.D., Hörrantner, M.T., Pazos-Outón, L.M., Lamboll, R.D., Ábolján, H., Leijtens, T., Mahesh, S., Friend, R.H., Snaith, H.J., Joyce, H.J., et al. (2019). Long-range charge extraction in back-contact perovskite architectures via suppressed recombination. *Joule* 3, 1301–1313.
  28. Hu, Z., Kapil, G., Shimazaki, H., Pandey, S.S., Ma, T., and Hayase, S. (2017). Transparent conductive oxide layer and hole selective layer free back-contacted hybrid perovskite solar cell. *J. Phys. Chem. C* 121, 4214–4219.
  29. Song, Y., Bi, W., Wang, A., Liu, X., Kang, Y., and Dong, Q. (2020). Efficient lateral-structure perovskite single crystal solar cells with high operational stability. *Nat. Commun.* 11, 274.
  30. Lin, X., Jumabekov, A.N., Lal, N.N., Pascoe, A.R., Gómez, D.E., Duffy, N.W., Chesman, A.S.R., Sears, K., Fournier, M., Zhang, Y., et al. (2017). Dipole-field-assisted charge extraction in metal-perovskite-metal back-contact solar cells. *Nat. Commun.* 8, 613.
  31. Hou, Q., Bacal, D., Jumabekov, A.N., Li, W., Wang, Z., Lin, X., Ng, S.H., Tan, B., Bao, Q., Chesman, A.S.R., et al. (2018). Back-contact perovskite solar cells with honeycomb-like charge collecting electrodes. *Nano Energy* 50, 710–716.
  32. DeLuca, G., Jumabekov, A.N., Hu, Y., Simonov, A.N., Lu, J., Tan, B., Adhyaksa, G.W.P., Garnett, E.C., Reichmanis, E., Chesman, A.S.R., et al. (2018). Transparent quasi-interdigitated electrodes for semitransparent perovskite back-contact solar cells. *ACS Appl. Energy Mater.* 1, 4473–4478.
  33. Jumabekov, A.N., Lloyd, J.A., Bacal, D.M., Bach, U., and Chesman, A.S.R. (2018). Fabrication of back-contact electrodes using modified natural lithography. *ACS Appl. Energy Mater.* 1, 1077–1082.
  34. Hu, Y., Adhyaksa, G.W.P., DeLuca, G., Simonov, A.N., Duffy, N.W., Reichmanis, E., Bach, U., Docampo, P., Bein, T., Garnett, E.C., et al. (2019). Perovskite solar cells with a hybrid electrode structure. *AIP Adv.* 9, 125037.
  35. Lin, X., Raga, S.R., Chesman, A.S.R., Ou, Q., Jiang, L., Bao, Q., Lu, J., Cheng, Y.-B., and Bach, U. (2020). Honeycomb-shaped charge collecting electrodes for dipole-assisted back-contact perovskite solar cells. *Nano Energy* 67, 104223.
  36. Jumabekov, A.N., Della Gaspera, E., Xu, Z.-Q., Chesman, A.S.R., van Embden, J., Bonke, S.A., Bao, Q., Vak, D., and Bach, U. (2016). Back-contacted hybrid organic-inorganic perovskite solar cells. *J. Mater. Chem. C* 4, 3125–3130.
  37. Maalouf, A., Gadonna, M., and Bosc, D. (2008). An improvement in standard photolithography resolution based on Kirchhoff diffraction studies. *J. Phys. D Appl. Phys.* 42, 015106.
  38. Grisaty, A., and Won, Y.H. (2014). Multi-layer insulator for low voltage and breakdown voltage enhancement in electrowetting-on-dielectric. In *Proceedings Volume 8987, Oxide-based Materials and Devices V (SPIE)*.
  39. Lin, Y.Y., Evans, R.D., Welch, E., Hsu, B.N., Madison, A.C., and Fair, R.B. (2010). Low voltage electrowetting-on-dielectric platform using multi-layer insulators. *Sens. Actuators B Chem.* 150, 465–470.
  40. Sahoo, S.K., Patel, R.P., and Wolden, C.A. (2013). Hybrid nanolaminate dielectrics engineered for frequency and bias stability. *J. Appl. Phys.* 114, 074101.
  41. Qin, J., Zhang, Z., Shi, W., Liu, Y., Gao, H., and Mao, Y. (2017). The optimum titanium precursor of fabricating TiO<sub>2</sub> compact layer for perovskite solar cells. *Nanoscale Res. Lett.* 12, 640.
  42. Grosvenor, A.P., Biesinger, M.C., Smart, R.S.C., and McIntyre, N.S. (2006). New interpretations of XPS spectra of nickel metal and oxides. *Surf. Sci.* 600, 1771–1779.
  43. Biesinger, M.C., Payne, B.P., Grosvenor, A.P., Lau, L.W.M., Gerson, A.R., and Smart, R.S.C. (2011). Resolving surface chemical states in XPS analysis of first row transition metals, oxides and hydroxides: Cr, Mn, Fe, Co and Ni. *Appl. Surf. Sci.* 257, 2717–2730.
  44. Biesinger, M.C., Lau, L.W.M., Gerson, A.R., and Smart, R.S.C. (2012). The role of the Auger parameter in XPS studies of nickel metal, halides and oxides. *Phys. Chem. Chem. Phys.* 14, 2434–2442.
  45. Ratcliff, E.L., Meyer, J., Steirer, K.X., Garcia, A., Berry, J.J., Ginley, D.S., Olson, D.C., Kahn, A., and Armstrong, N.R. (2011). Evidence for near-surface NiOOH species in solution-processed NiO<sub>x</sub> selective interlayer materials: Impact on energetics and the performance of polymer bulk heterojunction photovoltaics. *Chem. Mater.* 23, 4988–5000.
  46. Boyd, C.C., Shallcross, R.C., Moot, T., Kerner, R., Bertoluzzi, L., Onno, A., Kavadiya, S., Chosy, C., Wolf, E.J., Werner, J., et al. (2020). Overcoming redox reactions at perovskite-nickel oxide interfaces to boost voltages in perovskite solar cells. *Joule* 4, 1759–1775.
  47. Biesinger, M.C., Payne, B.P., Lau, L.W.M., Gerson, A., and Smart, R.S.C. (2009). X-ray photoelectron spectroscopic chemical state quantification of mixed nickel metal, oxide and hydroxide systems. *Surf. Interface Anal.* 41, 324–332.
  48. Li, Y.F., and Selloni, A. (2014). Mosaic texture and double c-Axis periodicity of β-NiOOH: Insights from first-principles and genetic algorithm calculations. *J. Phys. Chem. Lett.* 5, 3981–3985.
  49. Ming, W., Yang, D., Li, T., Zhang, L., and Du, M.H. (2017). Formation and diffusion of metal impurities in perovskite solar cell material CH<sub>3</sub>NH<sub>3</sub>PbI<sub>3</sub>: implications on solar cell degradation and choice of electrode. *Adv. Sci. (Weinh.)* 5, 1700662.

50. Islam, R., Chen, G., Ramesh, P., Suh, J., Fuchigami, N., Lee, D., Littau, K.A., Weiner, K., Collins, R.T., and Saraswat, K.C. (2017). Investigation of the changes in electronic properties of nickel oxide ( $\text{NiO}_x$ ) due to UV/ozone treatment. *ACS Appl. Mater. Interfaces* 9, 17201–17207.
51. Sun, Y., Chen, W., Wu, Y., He, Z., Zhang, S., and Chen, S. (2019). A low-temperature-annealed and UV-ozone-enhanced combustion derived nickel oxide hole injection layer for flexible quantum dot light-emitting diodes. *Nanoscale* 11, 1021–1028.
52. Klasen, A., Baumli, P., Sheng, Q., Johannes, E., Bretschneider, S.A., Hermes, I.M., Bergmann, V.W., Gort, C., Axt, A., Weber, S.A.L., et al. (2019). Removal of surface oxygen vacancies increases conductance through  $\text{TiO}_2$  thin films for perovskite solar cells. *J Phys Chem C Nanomater Interfaces* 123, 13458–13466.
53. Wang, Z., Fang, J., Mi, Y., Zhu, X., Ren, H., Liu, X., and Yan, Y. (2018). Enhanced performance of perovskite solar cells by ultraviolet-ozone treatment of mesoporous  $\text{TiO}_2$ . *Appl. Surf. Sci.* 436, 596–602.
54. Lee, H., Rhee, S., Kim, J., Lee, C., and Kim, H. (2016). Surface coverage enhancement of a mixed halide perovskite film by using an UV-ozone treatment. *J. Korean Phys. Soc.* 69, 406–411.
55. Stauss, S., Mori, S., Muneoka, H., Terashima, K., and Iacopi, F. (2013). Ashing of photoresists using dielectric barrier discharge cryoplasmas. *J. Vac. Sci. Technol. B* 31, 061202.
56. Yang, Z., Yang, W., Yang, X., Greer, J.C., Sheng, J., Yan, B., and Ye, J. (2020). Device physics of back-contact perovskite solar cells. *Energy Environ. Sci.* 13, 1753–1756.
57. Ma, T., Song, Q., Tadaki, D., Niwano, M., and Hirano-Iwata, A. (2018). Unveil the full potential of integrated-back-contact perovskite solar cells using numerical simulation. *ACS Appl. Energy Mater.* 1, 970–975.
58. Fang, G., Tian, H., Chang, W., Wang, Z., He, Q., and Gao, X. (2020). Optimized analysis of back-contact perovskite solar cells architectures. *Optik (Stuttg.)* 207, 164362.
59. Nardone, M., Spehar, M., Kuciauskas, D., and Albin, D.S. (2020). Numerical simulation of high-efficiency, scalable, all-back-contact  $\text{Cd}(\text{Se},\text{Te})$  solar cells. *J. Appl. Phys.* 127, 223104.
60. Demtsu, S.H., and Sites, J.R. (2006). Effect of back-contact barrier on thin-film CdTe solar cells. *Thin Solid Films* 510, 320–324.
61. Roussillon, Y., Karpov, V.G., Shvydka, D., Drayton, J., and Compaan, A.D. (2004). Back contact and reach-through diode effects in thin-film photovoltaics. *J. Appl. Phys.* 96, 7283–7288.
62. Bertoluzzi, L., Boyd, C.C., Rolston, N., Xu, J., Prasanna, R., O'Regan, B.C., and McGehee, M.D. (2020). Mobile ion concentration measurement and open-access band diagram simulation platform for halide perovskite solar cells. *Joule* 4, 109–127.
63. Sze, S.M., and Ng, K.K. (2006). *Physics of Semiconductor Devices* (John Wiley & Sons).
64. Liu, J., Gao, C., He, X., Ye, Q., Ouyang, L., Zhuang, D., Liao, C., Mei, J., and Lau, W. (2015). Improved crystallization of perovskite films by optimized solvent annealing for high efficiency solar cell. *ACS Appl. Mater. Interfaces* 7, 24008–24015.
65. Yi, A., Chae, S., Lee, H., and Kim, H.J. (2019). The synergistic effect of cooperating solvent vapor annealing for high-efficiency planar inverted perovskite solar cells. *J. Mater. Chem. A* 7, 27267–27277.
66. Meng, K., Wu, L., Liu, Z., Wang, X., Xu, Q., Hu, Y., He, S., Li, X., Li, T., and Chen, G. (2018). In situ real-time study of the dynamic formation and conversion processes of metal halide perovskite films. *Adv. Mater.* 30, 1706401.
67. Weber, S.A.L., Hermes, I.M., Turren-Cruz, S.-H., Gort, C., Bergmann, V.W., Gilson, L., Hagfeldt, A., Graetzel, M., Tress, W., and Berger, R. (2018). How the formation of interfacial charge causes hysteresis in perovskite solar cells. *Energy Environ. Sci.* 11, 2404–2413.
68. Saliba, M., Matsui, T., Seo, J.Y., Domanski, K., Correa-Baena, J.P., Nazeeruddin, M.K., Zakeeruddin, S.M., Tress, W., Abate, A., Hagfeldt, A., and Grätzel, M. (2016). Cesium-containing triple cation perovskite solar cells: improved stability, reproducibility and high efficiency. *Energy Environ. Sci.* 9, 1989–1997.
69. Perkins, C.L., and Hasoon, F.S. (2006). Surfactant-assisted growth of CdS thin films for photovoltaic applications. *J. Vac. Sci. Technol. A* 24, 497–504.
70. Payne, B.P., Biesinger, M.C., and McIntyre, N.S. (2011). X-ray photoelectron spectroscopy studies of reactions on chromium metal and chromium oxide surfaces. *J. Electron Spectrosc. Relat. Phenom.* 184, 29–37.
71. Baltrusaitis, J., Jayaweera, P.M., and Grassian, V.H. (2009). XPS study of nitrogen dioxide adsorption on metal oxide particle surfaces under different environmental conditions. *Phys. Chem. Chem. Phys.* 11, 8295–8305.